Analysis of Unbalanced Magnetic Pull of a Solid Rotor Induction Motor in a Waste Heat Recovery Generator

Rafal P. Jastrzebski, *Senior Member, IEEE*, and Adam K. Pilat, *Member, IEEE*

***Abstract*—In active magnetic bearing control systems, the performance of the closed-loop control and the application can be impaired by external disturbances. This article analyzes the unbalanced magnetic pull forces produced by the eccentricity of a high-speed 1MW 3-phase solid rotor induction motor. The effect of unbalanced magnetic pull on a five-degree-of-freedom active magnetic bearing control and the resulting vibrations are studied. Finite-element-method-based modeling of the electrical machine unbalanced magnetic pull and active magnetic bearing forces is carried out, and the results are used in the harmonic force analysis and modeling of an active magnetic bearing–rotor system. The overall engineering model comprising the rotor dynamics, unbalanced magnetic pull derived by the finite element method, active magnetic bearing forces, and the controller is tested by time-stepping simulations. The simulations and experimental results are reviewed. The severity of the unbalanced magnetic pull and its effects on the robustness of the active magnetic bearing closed-loop system in a hermetic steam turbogenerator applied in marine waste heat recovery systems are evaluated.**

***Index Terms*—Unbalanced magnetic pull, induction motor, magnetic levitation, digital control, vibration analyses, optimal control, active magnetic bearings, waste heat recovery system.**

I. Introduction

THE majority of applications for high-speed and high-power energy conversion systems rely on rotors supported by mechanical bearings with oil lubrication. However, maintenance costs and the need for hermetic solutions hamper the application of oil-film journal and ball bearings. Bearings are most important for the overall reliability of induction motors [1]. An unbalanced magnetic pull (UMP) from an eccentric rotor can decrease the traditional bearing lifetime. With time, an increasing number of high-speed applications start to employ contactless and frictionless bearing solutions, such as active magnetic bearings (AMBs) and bearingless motors. In the motor design process, determination of the rotor bending frequencies and the resulting critical speeds together with the rotor stresses and thermal effects define the limitations of the rotor construction and the system design. With the mechanical bearings, the UMP from the motor can only marginally change the critical speeds of short rotors [2]. However, for more gyroscopic but long rotors supported by AMBs, the considerable effects of UMP on vibrations have been measured [3]. Therefore, assessment of the anticipated UMP and its effect on the AMB feedback and stability are of importance. In the last decade, AMB-supported solid rotor induction motors (IMs) have been considered and employed in high-speed applications owing to their inherent robust mechanical and thermal properties [4], [5].

The AMB–rotor system is affected by motor-induced disturbances caused by electrical machine eccentric flux distribution but also because of electromagnetic interference and network distortions [6]. There are various reasons for the rotor eccentricity, including the rotor mass distribution [7], nonconcentric positioning of AMBs with the mechanical center clearance point and the center of the motor stator, manufacturing and assembly tolerances [8], bending of the rotor shaft, whirling at critical speeds, and load and external disturbances [9]. A rotor runout at position-sensor-measuring surfaces and at AMBs, and negative bearing stiffness combined with the effects of the controller on the rotor movement can produce considerable effects on the eccentric rotor motions [3]. For ball and roller bearings, the inner race, where the shaft rides, guides and constrains the eccentric motions. For AMBs, a clearance between the safety bearing race and the shaft is typically of half and above the average air gap. Harmonic forces are visible in AMB control feedback signals and control currents. Recordings of currents and displacements should be compared for the situations where the motor is turned off and on in order to separate the effects of UMP from the effects of runout and static rotor displacement from the bore center of AMBs. For high-speed AMB–rotors in the nominal AMB operating point, static eccentricity is present at the motor node. It occurs when the geometric rotor center is displaced from the stator bore center and the rotor is rotating about its geometric center. Combination of different disturbances as well as plant nonlinear dynamics make the analysis and measurements of eccentricity effects in industrial applications challenging. A

Manuscript received 6 June 2022; revised 26 October 2022; accepted 30 November 2022. Date of publication 8 December 2022; date of current version 23 May 2023. This work was supported in part by the Academy of Finland, under Grants 270012, 304071, 304784, and 350880. Paper no. TEC-00575-2022. *(Corresponding author: Rafal P. Jastrzebski.)*

Rafal P. Jastrzebski is with the Department of Electrical Engineering, Lappeenranta-Lahti University of Technology, 53850 Lappeenranta, Finland, and also with the Department of Mechanical and Materials Engineering, University of Turku, 20014 Turku, Finland, and also with the Aument Power Oy, Finland (e-mail: rafal.jastrzebski@utu.fi).

Adam K. Pilat is with the AGH University of Science and Technology, Faculty of Electrical Engineering, Automatics, Computer Science and Biomedical Engineering, Department of Automatic Control and Robotics, 30-059 Krakow, Poland (e-mail: ap@agh.edu.pl).

Color versions of one or more figures in this article are available at https://doi.org/10.1109/TEC.2022.3227551.

Digital Object Identifier 10.1109/TEC.2022.3227551

This work is licensed under a Creative Commons Attribution 4.0 License. For more information, see https://creativecommons.org/licenses/by/4.0/

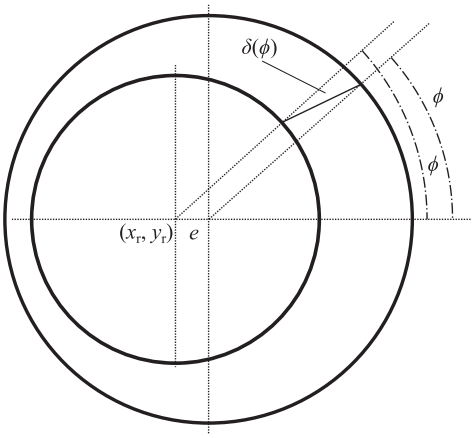

Fig. 1. Supported rotor with the eccentricity e.

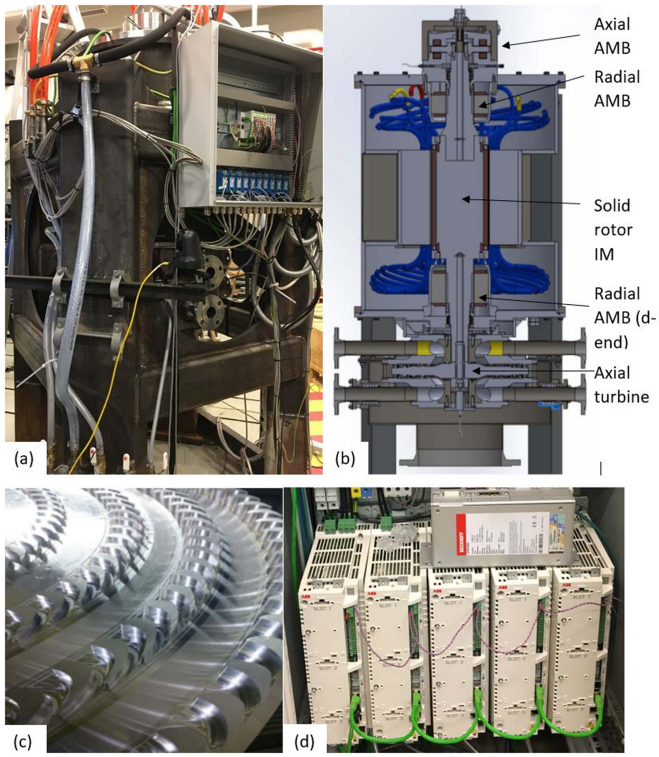

Fig. 2. (a) Laboratory prototype of the 1 MW hermetic turbogenerator, by courtesy of Aument Power Oy, with pipes for the internal shaft water cooling and the position sensor drivers in the connection box. (b) Cross section. (c) Axial turbine. (d) AMB control electronics [22][5].

more detailed insight into UMP and other disturbance effects on the AMB control is important not only for control tuning and actuator scaling but also for machine-, mechanical-, and system-level designs, and application feasibility.

Modeling and assessment of harmonic forces on eccentric rotors in electrical machines have been performed with analytical methods [10]. UMP analytical models of cage rotor IMs have been described in [7], [11], [12], [2], and [13], where slot harmonics have been included. Furthermore, eccentricity diagnostics based on the harmonic analysis and the finite element method (FEM) has been performed [9]. Fernandez Gomez et al. [14] developed analytical harmonic models for eccentric IMs. Empirical methods were applied for the same task by Chuan et al. [15]. Echeverria et al. [16] analyzed UMP in large machines, and Salah et al. [17] provided a comprehensive review of UMP diagnostics and damping for IMs. However, studies on UMP and the resulting vibrations have focused on nonsolid rotors with mechanical bearings and nominal operating conditions. For a solid rotor, accurate field computation has been more challenging because of the eddy currents [18].

This work addresses a number of research questions. What is an effective technique to compute and measure the UMP of a solid rotor? What do the harmonic forces look like in different operating conditions? How can practical models of UMP forces be constructed for extended control simulations on UMP effects and their influence on the AMB–rotor system being controlled?

The application area of the case study proof of concept, employed to answer the research questions, is a marine waste heat recovery system (WHRS). Moreover, the proof of concept is also suitable for steam turbines and power station engines used in electricity production.

For proofs of concept of high-power high-speed electrical machines, there is very little room for system design errors. The contributions of this paper, relative to the current state of the art, are in the proposed methods of modeling and measuring UMP, and simulating its effects on AMB–rotors. The effects of eccentricity in an AMB-supported hermetic turbogenerator are studied. A method is presented to compute in 2D FEM the UMP of a solid rotor induction machine with significant saturation and eddy current effects. Based on computed forces, a comprehensive harmonic analysis of the UMP in various working conditions is performed. Furthermore, the results are used together with nonlinear multi-input multi-output electromechanical AMB–rotor models to introduce an accurate engineering proof of concept model capable of simulating UMP effects as well as the effects of other disturbances on the AMB closed-loop control implementation in various scenarios. With the proposed models, the system, component, and control designs can be validated. In particular, the presented UMP and AMB force engineering models provide an alternative to, e.g., empirical models [15]. With built-in position sensors, which are necessary for AMB feedback, harmonic vibration effects are analyzed with simulations and experimental data.

II. Electromagnetic Forces in an AMB–Rotor System

The AMB and UMP forces in the AMB-supported IM rotor (Fig. (2)) applied to a WHRS are studied. Concise analytical principles are followed by details of the FEM. The results are later applied to simulations and compared with experiments.

A. UMP Forces

For induction motor UMP, the radial force components (e.g., based on [10]) can be computed as a function of the radial air-gap magnetic flux density $B_\delta(\phi)$ by simplifying the integrals of the Maxwell stress tensor around the rotor with the diameter D_r and

the stack length L_s as

$$f_x = \int_0^{2\pi} \frac{B_\delta(\phi)^2}{4\mu_0} D_\mathrm{r} L_\mathrm{s} \cos\phi d\phi, \quad (1)$$

$$f_y = \int_0^{2\pi} \frac{B_\delta(\phi)^2}{4\mu_0} D_\mathrm{r} L_\mathrm{s} \sin\phi d\phi, \quad (2)$$

where μ_0 is permeability of vacuum, and $\phi \in [0, 2\pi]$ is the rotor angular position.

The flux density can be solved as a function of the air-gap permeance $\lambda(\phi)$ and the magnetomotive force (MMF) $\mathcal{F}(\phi)$ in the air gap

$$B_\delta(\phi) = \lambda(\phi)\mathcal{F}(\phi). \quad (3)$$

The rotor position in the stator bore, the stator, and the rotor slotting modify the air-gap permeance, which can be approximated using Carter factors [19], [10]. The rotor k_Cr and stator k_Cs Carter factors result in a reduced mean magnetic flux density over the slots

$$\lambda(\phi) = \frac{\mu_0}{\delta(\phi) k_\mathrm{Cr}(\phi) k_\mathrm{Cs}(\phi)}, \quad (4)$$

where $\delta(\phi)$ is the radial air gap. For the rotor center displaced by x_r and y_r from the stator bore center, the air gap calculated as the distance between the points on the inner stator surface with the diameter D_s and the points on the outer rotor circle with the diameter D_r at ϕ can be computed, e.g., as in Fig. 1

$$\delta(\phi) = \sqrt{(x_\mathrm{r} + \delta_0 \cos\phi)^2 + (y_\mathrm{r} + \delta_0 \sin\phi)^2}, \quad (5)$$

where $\delta_0 = (D_\mathrm{s} - D_\mathrm{r})/2$ is the nominal air gap. Alternatively, the air gap can be approximated as a distance between the points on the stator and rotor circles and the line going through the center of the stator $\delta(\phi) = \delta_0 - e\cos\phi$ [10] [11] or the rotor [20]. For the eccentricity $e \to 0$, all the above-mentioned formulations yield identical results. The MMF and permeance are typically expanded for instance as Taylor series functions [10], [11]. However, with the saturation effects of high air-gap flux densities and eddy-current effects, especially for solid rotors, accurate force computation, which would include all slot and bar induced harmonics, is very challenging [21], [12]. Analytical or empirical methods are case-sensitive and require tuning to FEM results or experimental results. Here, 2D FEM-based (Fig. 3) results are used directly to construct engineering models.

First, the machine under no load, and at a very small slip $=$ 0.00001 that is necessary to overcome rotor losses and windage losses, is studied (Fig. 4). Static eccentricities up to 50% of the nominal air gap (Table I) are considered. Gradual variable time stepping of 1.2 s (with a time step change of no more than half of the time step in the previous revolution) to reach solid rotor steady-state magnetization under eddy currents is applied. The rotor motion is constrained to integer numbers in degrees. The last 360 steps at a 1 $^\circ$ accuracy are used for the harmonic analysis. The steady states are reached after 2245 steps. The selected case was simulated and the result trends were confirmed in the Maxwell software in addition to the JMAG one. For solid parts and high signal amplitudes, there is a significant time delay in the rotor iron magnetization caused by eddy currents, and the time constant is highly dependent on the amplitude of the MMF.

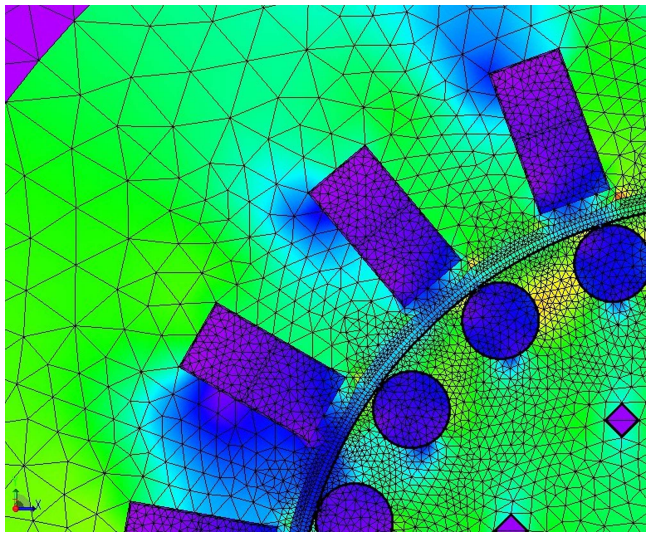

Fig. 3. Details of motor meshing with 37500 elements, a 4-layer skin mesh on the rotor surface, and a 3-layer sliding mesh with 720 circumferential divisions in the air gap.

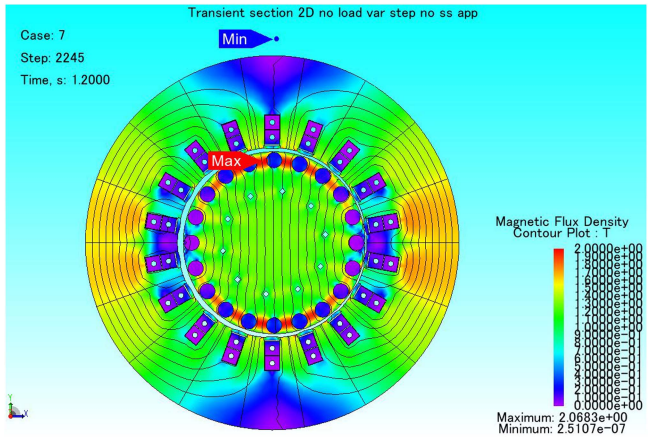

Fig. 4. Flux lines and a contour plot at slip $=$ 0.00001 and rated current.

The resulting mechanical speed harmonics of the UMP forces are shown in Fig. 5. In the figure, the amplitudes increase with eccentricity as indicated by shades of brown for different left and right scales. For the nominal phase current, the mean force and the 18th harmonics roughly double, but the 1st harmonic decreases, compared with the case with one-third of nominal current. The dc values, rotor pole, and stator slot harmonics are dominant. Harmonics related to the number of bars are less significant. At the 2 mm eccentricity (40% of the IM air gap), the zero harmonic UMP force would exceed the force capacity of the upper AMB, resulting in a touchdown. Second, the machine under nominal load, which is defined at the constant slip $=$ 0.0019 and the phase current amplitude $I_\mathrm{a,ph} = 1646$ A, is studied. The slip results in eddy currents, which reduce the flux penetration of the rotor surface and bend the flux lines in the solid rotor (Fig. 7 vs. 4). The resulting mechanical speed harmonics are shown in Fig. 8. The 1st harmonic and the dc value are reduced compared with the no-load case. The higher

TABLE I
MAIN PARAMETERS OF THE 1MW 12500 R/MIN INDUCTION MACHINE

Parameter	Parameter value
Number of rotor bars (stator slots)	20 (18)
Number of pole pairs	1
Number of slots per pole and phase	3
Rated frequency	12500/60 Hz
Nominal air gap	5 mm
Rated stator phase current	1164 A
Stator core material	M-270-50 A
Rotor material	X20Cr13
Rotor mass	265 kg

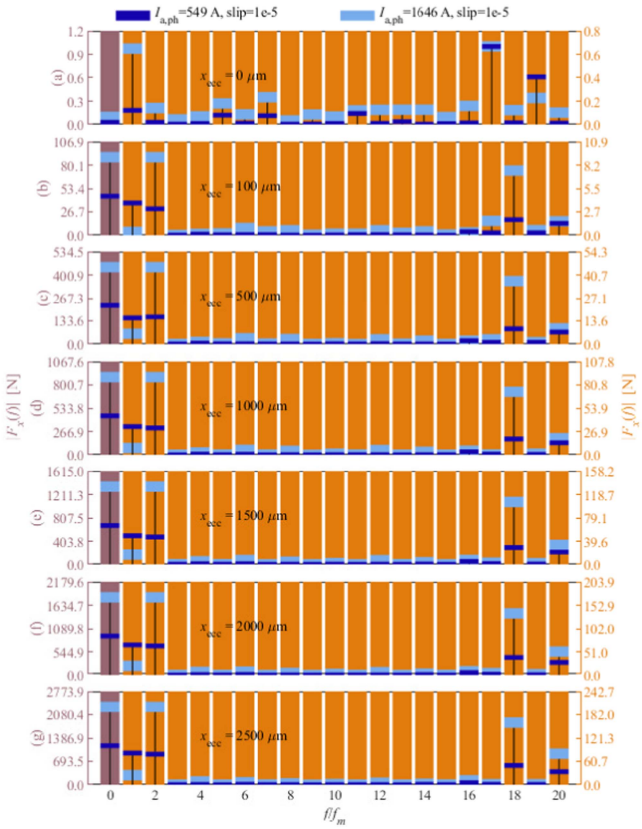

Fig. 5. Force harmonics in the eccentricity direction at slip = 0.00001.

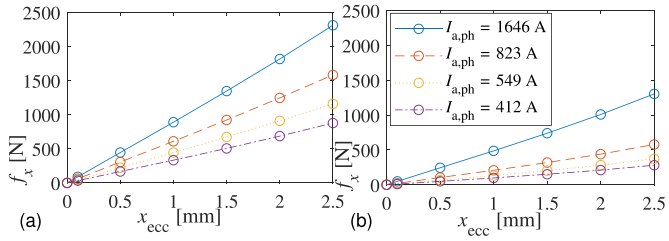

Fig. 6. Mean force in the eccentricity direction at (a) slip = 0.00001 and (b) 0.0019 at various motor phase currents. The static eccentricity results in a zero harmonic perceived as a negative stiffness by the AMB–rotor system in the location of the motor.

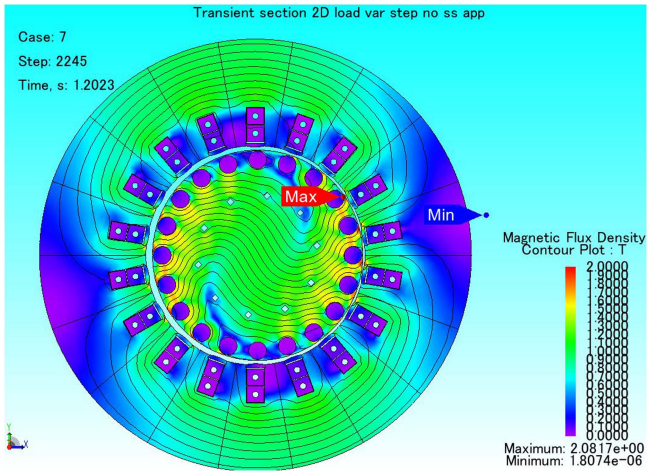

Fig. 7. Flux lines and a contour plot at slip = 0.0019 with rated current.

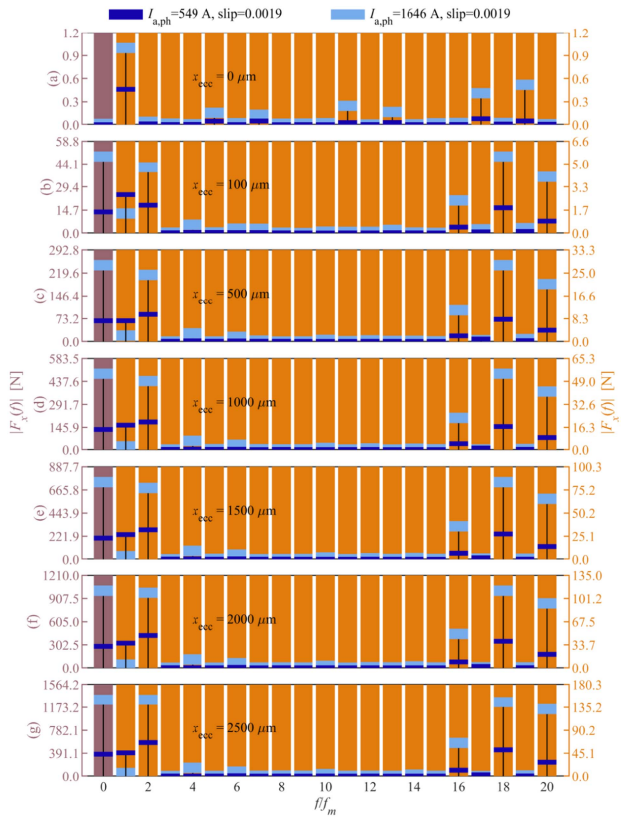

Fig. 8. Force harmonics in the eccentricity direction at slip = 0.0019.

force harmonics are changed compared with the low slip (no torque) case.

The presented simulation method works for static eccentricity but also with stable limit cycle motions, such as dynamic and mixed eccentricities. The measured instantaneous torque has also harmonic content, which is dependent on the eccentric position.

TABLE II
MAIN PARAMETERS OF THE UPPER N-END (LOWER D-END) RADIAL AMB

Parameter	Parameter value
Number of E-cores per AMB	4
Nominal air gap	1.15 mm
Nominal clearance	0.4 mm
Stator lamination material	M-270-50A
Rotor lamination material	Sura No10
Force capacity upper (lower)	1130 (1793) N
Maximum rated control current $i_{c,\max}$	10 A
Rated bias current i_b	7.66 A
Large signal inductance upper (lower)	0.0204 (0.031) H
Large signal bandwidth upper (lower)	272 (180) Hz
Large signal current stiffness upper (lower)	131 (207) N/A
Large signal position stiffness upper (lower)	1271 (2017) N/mm

B. AMB Forces

For the complete modeling of the electromagnetic forces acting on the rotor, the AMB forces are derived.

AMB force generation phenomena can be described applying the principles of virtual work [23] followed by energy or coenergy derivation; coenergy is preferred because of the more straightforward expressions of winding currents and inductances for most systems. The force as a function of the radial air-gap magnetic flux density B equals the partial derivative of the magnetic coenergy W_{ce} with regard to the virtual displacement l:

$$f = \frac{\delta W_{ce}}{\delta l} = \frac{B^2 S_{air} \cos \xi}{\mu_0} \tag{6}$$

where ξ is the AMB geometry-specific force-acting angle. S_{air} is the equivalent pole area of one electromagnet. The average magnetic flux density solved from the AMB magnetic circuit of a single electromagnet when neglecting fringing and leakage effects can be approximated as

$$B = \frac{\mu_0 N i}{l_{Fe}/\mu_{Fe} + 2l_{air}} \tag{7}$$

where l_{Fe}, l_{air}, μ_{Fe}, N, and i are the flux path lengths in the iron and air, the relative permeability of iron, the AMB coil turn number, and the coil current, respectively. The radial AMB geometry comprising four electromagnets, where the same coils accommodate both the bias and control currents (Table II), is shown in Fig. 9. The selected reduced bias is a compromise between the force linearization (preferably a high bias current $i_b = i_{c,\max}$), the current density in the AMB windings (preferably a low bias), and noise propagating to the position sensors because of the power switches (preferably a low bias).

The bottom-end AMB (Fig. 2(b)) has a greater force capacity because of the location of the turbine wheel. In the FEM, similar to the IM model, the sliding mesh and eccentricity conditions are used. The forces and inductances of the AMBs are solved for variable coil and control currents and displacements of the rotor in the AMB plane (Fig. 10). The engineering Lookup Table (LUT) models of forces and inductances are built based on the

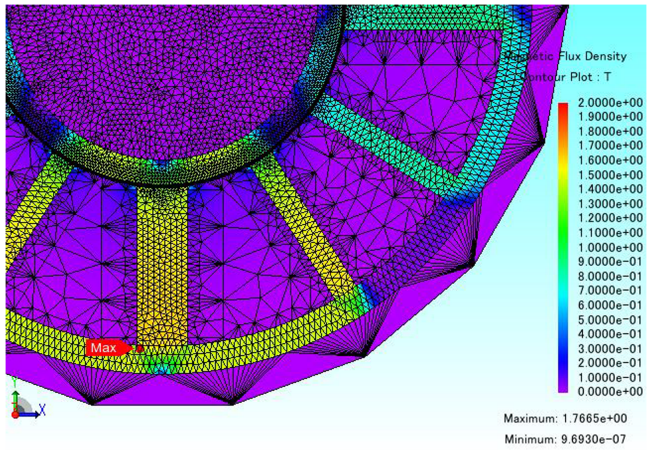

Fig. 9. Radial AMB FEM model with mesh and magnetic flux density contour results for the maximum rated control current applied in the y-axis E-core electromagnets and for the rated bias currents in all the E-core electromagnets.

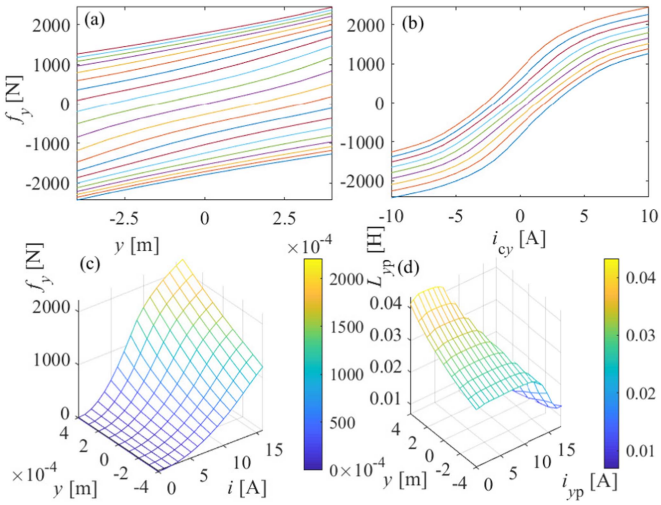

Fig. 10. Force and inductance fields of the radial d-end AMB. (a) $f_y(y)$ for the control current $i_c \in <-10, 10>$ A. (b) $f_y(i_{cy})$ for $y \in <-0.3, 0.3>$ mm. (c) $f_y(i, y)$ of one electromagnet and no bias. (c) The inductance $L_{yp}(i_{yp}, y)$ of the electromagnet on the positive y-axes and no bias.

FEM results. Because of the relatively large air gap (but a small clearance), the force and inductance position dependence is more linear than the current dependence. The rotor axial motion is controlled by the axial AMB. In this work, the radial and axial dynamics are considered to be decoupled from each other. This is valid for nonconical AMBs and for the stiff frame.

III. CLOSED-LOOP ROTOR SIMULATIONS WITH UMP

The overall simulation model of the AMB–rotor system and UMP can be used for the evaluation of the control, design iterations, assessment of the effects of the UMP, unbalance, runout, nonconcentric assembly, or other various disturbances or faults (Fig. 11).

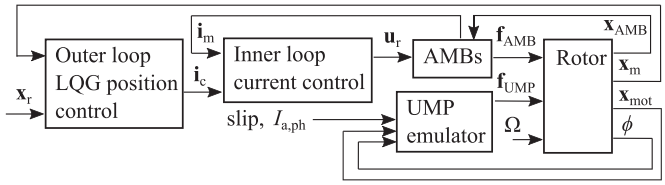

Fig. 11. Block diagram of the simulation model. Rotor displacement vectors from the central position are measured at the AMB locations $\mathbf{x}_{\mathrm{AMB}}$, motor stator location $\mathbf{x}_{\mathrm{mot}}$, and position sensor locations $\mathbf{x}_{\mathrm{m}}$.

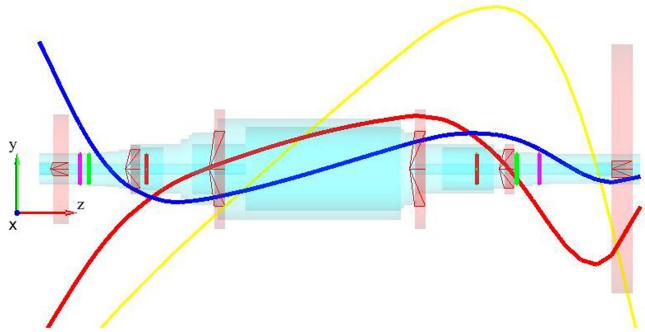

Fig. 12. Beam rotor model with added discs and mode shapes of the first three lowest frequency bending modes (149.7 Hz, 376.6 Hz, 627.2 Hz). With cooling water inside the model, the frequencies shift to (149.5 Hz, 375.5 Hz, 623.8 Hz).

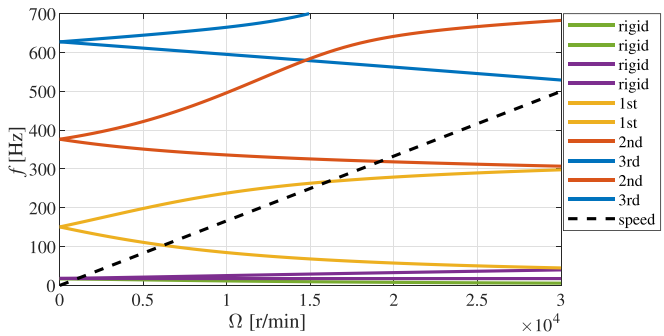

Fig. 13. Campbell diagram of the rotor with four rigid and six bending modes.

A. AMB–Rotor Model

The AMB model comprises LUT-based force and inductance tables (dependent on eccentric displacements at the corresponding planes and coil currents) derived from the FEM (Fig. 10(c) and (d)), inner AMB current-control loops [24], PWM, and transportation delays. Static FEM simulations are used for the derivation of LUTs. The forces of AMBs enter the speed-dependent mechanical model (Fig. 12) through the bearing planes. The AMB model requires positions and velocities of the rotor measured at bearing planes.

The mechanical model comprises the rigid rotor modes and the FEM-derived first six lowest frequency rotor bending modes (Fig. 13). In the modal coordinates, the modal displacement vector $\mathbf{x}$ follows a rotational speed Ω dependent generalized

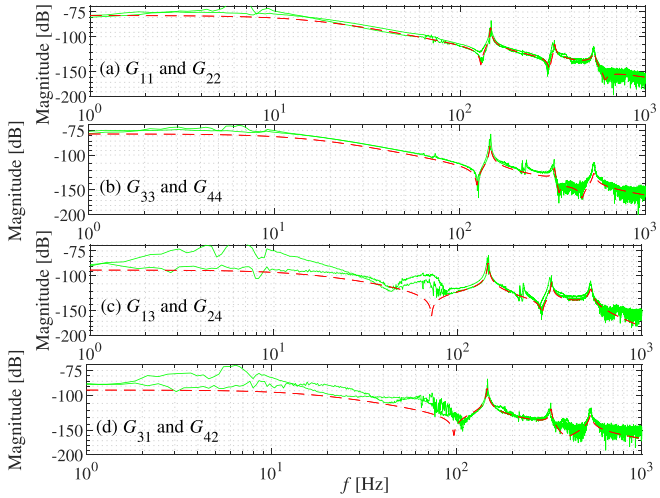

Fig. 14. Measured magnitude Bode plots of the AMB–rotor system (green) compared with magnitude plots of the transfer function $\mathbf{G}$ of the tuned radial plant (red). (a) $i_{cx_n} \rightarrow x_n$ and $i_{cy_n} \rightarrow y_n$ on the axial disc side. (b) $i_{cx_d} \rightarrow x_d$ and $i_{cy_d} \rightarrow y_d$ on the turbine wheel side. (c) $i_{cx_d} \rightarrow x_n$ and $i_{cy_d} \rightarrow y_n$. (d) $i_{cx_n} \rightarrow x_d$ and $i_{cy_n} \rightarrow y_d$.

form

$$\mathbf{M}\ddot{\mathbf{x}} + (\mathbf{D} + \Omega\mathbf{G})\dot{\mathbf{x}} + \mathbf{K}\mathbf{x} = \mathbf{f}, \tag{8}$$

where $\mathbf{M}$, $\mathbf{D}$, $\mathbf{G}$, $\mathbf{K}$, and $\mathbf{f}$ represent the modal mass, damping, gyroscopic, and stiffness matrices and the vector of external forces, respectively. $\mathbf{x}$ comprises the amplitudes of the rigid rotor modes (in center of gravity coordinates) and k the bending rotor modes. $\mathbf{x}$= $[x \quad y \quad \varphi_x \quad \varphi_y \quad x_1 \quad y_1 \quad \ldots \quad x_k \quad y_k]^{\mathrm{T}}$.

The effects of the frame and the base could have been taken into account in the modeling. However, they have not been significant in the tested machine. Input and output transformation matrices, including rotor vector displacement from the stator bore center measured from the flexible rotor beam model, displacements in the bearing and sensor locations, force inputs entering the motor (divided into two halves to take account of the stator length), and the AMB locations are used. External disturbance forces, UMP forces, runout, and sensor and actuator noise can be entered through the model inputs, each with a corresponding coordinate transformation.

The final mechanical models and cascaded control [25], [24] are tuned according to the identification results (Fig. 14) at a standstill. In the rotor model, the modal damping, stiffness, and masses are tuned to fit the resonance peaks. The rigid body mass properties are assumed known. The mode shapes are tuned to fit the resonances, antiresonances, and cross-coupling terms. The detailed time-continuous plant (often referred to as a virtual prototype in the recent literature) is tested with a digital controller, as it would have been implemented in the real control system.

The radial position control plant is a 16th-order system. The centralized radial model-based adaptive controller (and observer), comprises a rotor retaining four rigid modes and two bending modes, linearized AMB forces, and approximated

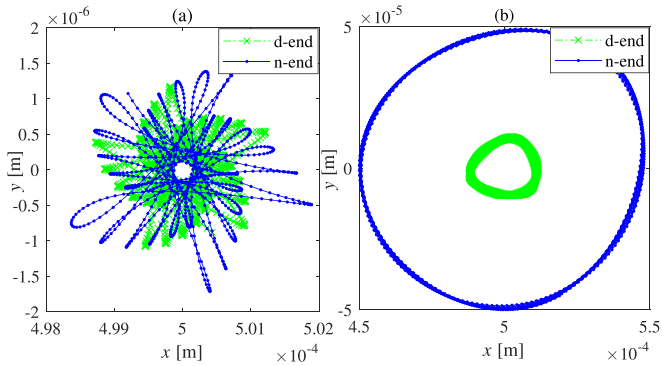

Fig. 15. Simulated no-load d-end and n-end radial rotor positions for $x_{\mathrm{ref}} = 0.5$ mm and $f = 60$ Hz. (a) Motor turned off, $I_{\mathrm{ph}} = 0$ A. (b) Motor turned on, $I_{\mathrm{ph}} = 1646$ A.

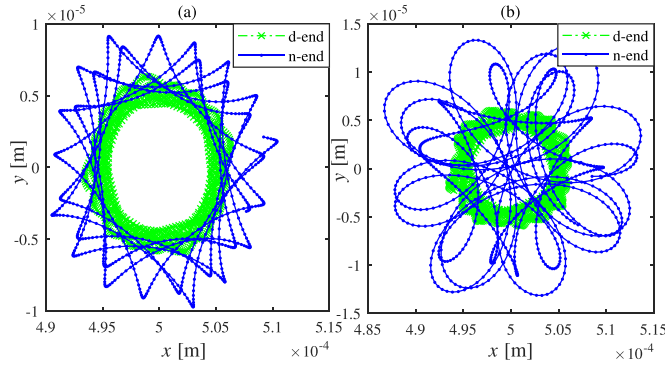

Fig. 16. Simulated no-load d-end and n-end radial rotor positions for $x_{\mathrm{ref}} = 0.5$ mm and $f = 200$ Hz. (a) Motor turned off, $I_{\mathrm{ph}} = 0$ A. (b) Motor turned on, $I_{\mathrm{ph}} = 1646$ A.

dynamics of the inner current control loops with PWM, signal transportation, and measurement delays.

Further modeling details of the AMB–rotor system, nonlinear rotor dynamics, identification, mass unbalance, and control design are beyond the scope of this paper.

B. UMP Model

From a series of time-stepping FEM simulations, the UMP engineering model is derived. The UMP model topology comprises xy input rotor displacement vectors of the rotor measured at two equal stator halves (indicated by A and B), transformed into polar coordinates with the eccentricity phase $\phi_{\mathrm{e}} = \mathrm{mod}(\mathrm{cart2pol}(x_{\mathrm{r}}, y_{\mathrm{r}}), 2\pi)$ and the amplitude $x_{\mathrm{ecc}} = \sqrt{(x_{\mathrm{r}}^2 + y_{\mathrm{r}}^2)}$, UMP force LUTs (dependent on the eccentric displacement, phase current, and rotor angle) $\mathbf{f}_{\mathrm{LUT}}(x_{\mathrm{ecc}}, I_{\mathrm{a,ph}}, \phi_{\mathrm{e}})$, and rotation of the forces in the xy plane counterclockwise through an eccentricity angle using the rotation matrix $\mathbf{R}$. Linear interpolation is applied between the breakpoints of all LUTs. The vector of UMP forces

$$\mathbf{f}_{\mathrm{UMP}} = \frac{1}{2}\begin{bmatrix} \mathbf{R}(\phi_{\mathrm{e,A}}) \cdot \mathbf{f}_{\mathrm{LUT}}(x_{\mathrm{ecc,A}}, I_{\mathrm{a,ph}}, \phi_{\mathrm{e,A}}) \\ \mathbf{R}(\phi_{\mathrm{e,B}}) \cdot \mathbf{f}_{\mathrm{LUT}}(x_{\mathrm{ecc,B}}, I_{\mathrm{a,ph}}, \phi_{\mathrm{e,B}}) \end{bmatrix}, \quad (9)$$

$$\mathbf{R} = \begin{bmatrix} \cos(\phi_{\mathrm{e}}) & -\sin(\phi_{\mathrm{e}}) \\ \sin(\phi_{\mathrm{e}}) & \cos(\phi_{\mathrm{e}}) \end{bmatrix}. \quad (10)$$

Static eccentricity has been dominant in the experiments with tightly controlled air-gap vibrations and the unbalanced force rejection control turned on. Therefore, the UMP model is accurate for small dynamic eccentricities including the effect of slot harmonics. The model accuracy can be further improved by including the influence of the relative position of slots vs. the eccentricity angle if greater dynamic eccentricity (with respect to the machine air gap) effects are to be tested (including effects of modulated slot and rotor bar harmonics). Any UMP model will be limited by the changes of solid rotor magnetization in time for very high variations of eccentricity.

Figs. 15 and 16 show rotor position orbits recorded from the sensor locations in the eccentric position and compared for the

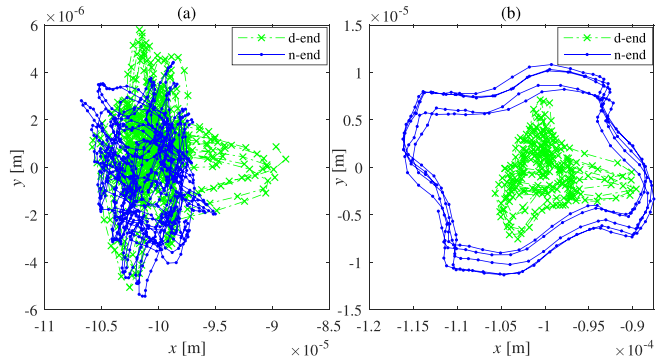

Fig. 17. Measured d-end (lower, i.e., turbine end) and n-end (upper) radial rotor positions at the -0.1 mm reference at various speeds. (a) $f = 60$ Hz. (b) $f = 180$ Hz.

motor turned on and off. The simulations assume a perfectly balanced rotor, no aerodynamic forces, no runout, and no measurement or actuator noise. The figures present the last stage of the simulation under steady-state orbits. The UMP forces have a higher impact at lower speeds. With increased eccentricity, the vibration amplitude increases. The first harmonic vibrations will also increase when operating close to the critical speed.

IV. Experimental Results

First, tests at a constant rotational speed ($\Omega = 2\pi \cdot 180$ rad/s) for different reference positions are performed. Motor forces overcome drag forces mostly coming from the turbine wheel. Modeling and identification of the aerodynamic forces of the turbine is outside the scope of this work. However, their effect is present in the measurements. Fig. 17 shows measured position orbits at the -0.1 mm reference (assumed eccentricity) applied at the both AMBs. For the measured medium and high speeds, the eccentricity is mostly static at the sensor planes. Slight rotor whirling with the 1st fundamental appears at higher speeds. It could result from approaching the forward first bending mode (Fig. 13) and nonidealities in the gyroscopic effect modeling in the controller. Fig. 18 shows measured force harmonics in

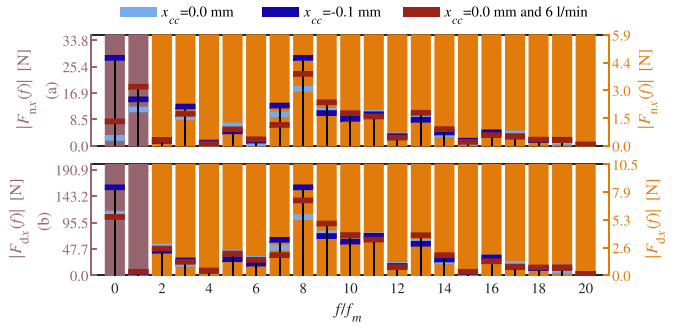

Fig. 18. Experimentally measured force harmonics at $I_{\mathrm{a,ph}} = 368$ A, $f = 180$ Hz, and moment 10% at the zero eccentricity $x_{\mathrm{ecc}} = 0$ with and without cooling (6 l/min cooling water flow inside the rotor), and at $x_{\mathrm{ecc}} = -0.1$ mm without cooling.

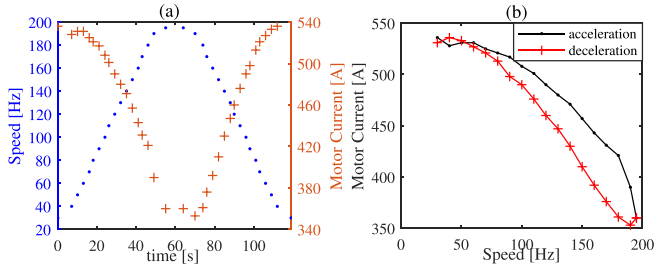

Fig. 19. Run-up/down speed test for the rotor placed in the reference position -0.1 mm recorded at both the radial displacement sensor planes. The rotor torque is in the range of 0.1 to 0.15% of the nominal value during the run-up acceleration and in the range of -0.02 to 0.02% of the nominal value during the run-down deceleration. The motor current and speed were recorded from a Vacon inverter.

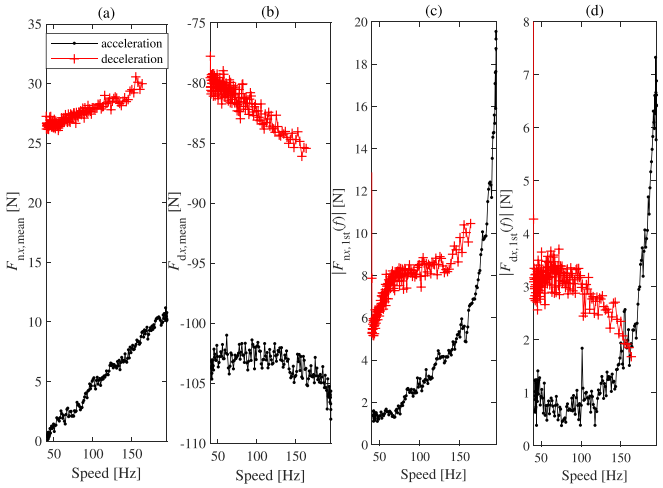

Fig. 20. Measured mean forces (ab) and the 1st rotational speed harmonics (cd) in the reference position -0.1 mm.

zero and -0.1 mm reference positions. The xy force vectors in the bearing locations are measured using the AMB control currents i_{c} and estimated rotor positions in the location of the bearings. For example, $f_y = k_i i_{cy} + k_y y$. k_i and k_y are the linearized current stiffness and the position stiffness in the operating point. For more accurate measurements of the UMP forces in particular, the forces could have been estimated in the location of the IM for example by an observer, which would have been running in real time as part of the model-based controller or in parallel to it. Fig. 18 shows that the force harmonics change because of the presence of a 6 l/min water flow cooling the rotor. For ideal manufacturing and a uniform water distribution, according to the rotor FEM simulations, the rotor balancing and dynamics are not significantly affected by the presence of water (Fig. 12). The rotor is balanced to G2.5 in order to comply with [26]. However, for instance the 1st and 8th harmonics are considerably different. This could also result from differences in the temperature distributions and the thermal expansion. The lower 1st harmonic compared with the FEM is an effect of the measured force location at the AMBs and not at the IM stator location as well as effects of aerodynamic forces and gyroscopic self-centering. The dc forces change with a change in the reference position.

Tests without the electrical machine being turned on are challenging because of significant air friction. Air drag from the turbine wheel causes the rotor speed to vary nonlinearly, which introduces errors to the FFT computations as a function of speed despite windowing [27]. Instead, a run-up and run-down speed test for the rotor placed in the reference position -0.1 mm is performed. Fig. 19 shows speeds and motor currents during the test. In Fig. 20, the mean forces and the 1st rotational speed harmonics are compared for the rotor accelerating at a constant rate and the decelerating rotor. The higher values of the mean forces and the 1st harmonics during deceleration (at a lower moment and slip) confirm the FEM results on UMP (e.g. Fig. 5(b) vs. Fig. 8(b)). The 1st harmonics during deceleration are higher despite lower phase currents. The higher harmonics are attenuated by the inertia of the high-speed rotor and the low signal-to-noise ratio for a small practical achievable eccentricity.

V. Discussion

So far, we have focused on the static eccentricity. Here, we briefly address a mixed eccentricity case comprising both static and dynamic eccentricities. For the case of the two-pole magnetized rotor in a dynamic eccentricity state, the eccentric direction is aligned with the magnetization direction. The measured orbits and forces at the n-end from Figs. 17 and 18 correspond to the mixed eccentricity case with the $x_{\mathrm{ecc,s}} = 0.1$ mm static eccentricity and, in addition, the small $x_{\mathrm{ecc,d}} = 0.01$ mm dynamic eccentricity. For example, in the JMAG 18-21 FEM, this can be replicated by setting the rotor part offset to 0.11 mm and the rotation axis offset to 0.1 mm. For this mixed eccentricity case, using variable time stepping and longer simulation times, e.g., 2 s dissipates eddy current effects on the transient in the iron magnetization. For small eccentricity values, the FFT requires a sufficient number of steps. Here, two final rotor revolutions with steps at every 0.5 ° are used.

For the eccentricity case present in the measurements (static 0.1 mm and dynamic 0.01 mm) and for the exaggerated eccentricity (static 1 mm and dynamic 1 mm), the FEM points to

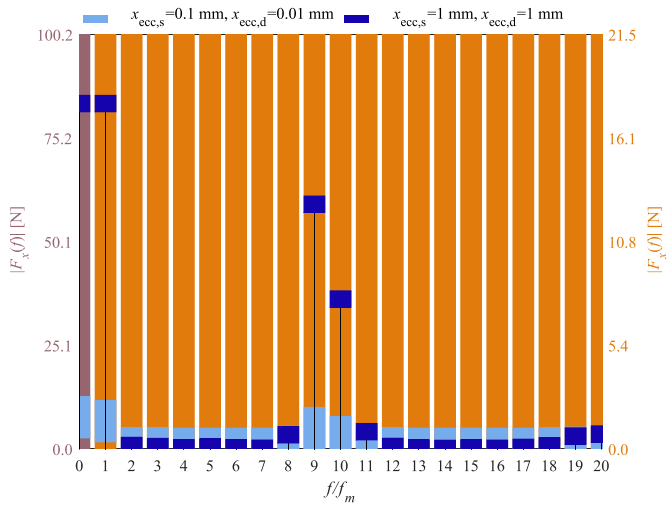

Fig. 21. FEM-computed force harmonics at $I_{\mathrm{a,ph}} = 368$ A, $f = 180$ Hz, and moment 10% (of nominal) for the mixed eccentricity cases: static 0.1 mm plus dynamic 0.01 mm (corresponding to the eccentricity case in Fig. 18), static 1 mm plus dynamic 1 mm (exaggerated case with large eccentricity values).

the existence of the zero, first, and eight through eleventh UMP force harmonics as seen in Fig. 21. The zero, first, and eight harmonics are also larger for the measured mixed eccentric case compared with the assumed noneccentric case in Fig. 18(a).

The experimentally measured conditions had a very small eccentricity relative to the air gap. There are, however, other forces acting on the rotor in the experiment, such as turbine forces related to the turbine hub / turbine construction and possible fluid spatial pressure differences. Additionally, water cooling inside the rotor can cause uneven and dynamic mass distribution in various temperature conditions. The FEM results are limited by the mesh, computation accuracy, and 2D structure, and therefore, all multiphysical effects cannot be taken into account in the simulation, and a comparison between the experiment and the FEM/simulation is challenging for relatively (to the air gap) small eccentricity values.

The experimental orbits are measured at the sensor planes while the UMP forces enter the motor location. Therefore, the force amplitudes from the motor FEM are not directly comparable with the forces measured experimentally. In order to take account of the bending modes, the displacements at the bearing locations would have to be estimated by using, e.g., a Kalman filter. The estimation would be limited in the presence of unknown nonstochastic disturbances and plant model parameter discrepancies and nonlinearities; furthermore, those effects cannot be separated. In the simulation model, the UMP forces entering the location and the measurement planes are like in the experiment where the physical locations of the motor and the sensors are. However, the simulation model does not include all external disturbances, e.g., turbine forces and mass unbalance forces.

In general, we have two unbalance effects: a mass unbalance and the motor UMP effects. The mass unbalance is assumed small according to the balancing grade, but with water cooling it is unknown. It will generate the first harmonic forces and rotor vibrations. We have neglected it in the simulations, but it is there and will obscure comparisons.

The motor UMP force is included in the LUT model derived from the FEM and inserted into the simulation model. In the experimental results we have not attempted to translate measured/estimated bearing forces into measured/estimated motor UMP forces because of the small relative eccentricity and other disturbances.

Motor UMP forces are acting relatively close to the center of gravity (COG) of the rotor. The static eccentricity of the motor would result mostly in COG translations. Let us assume that a stator center having a cooling channel in the middle has the rotor COG going exactly through that channel. If only a translation displacement of the rotor with static eccentricity is present, the motor UMP from two motor halves creates overturning moments that, because of gyroscopic effects, cancel each reaction moment. This can be verified by the gyroscopic effect principle that torque, e.g., $\boldsymbol{\Theta}$ applied perpendicular to the principal axis of rotation z and the principle momentum $\mathbf{L}_z = I_z\Omega$ (with the mass moment of inertia I_z), results in an angular velocity $\dot{\beta}$ perpendicular to both $\boldsymbol{\Theta} = \dot{\beta} \times \mathbf{L}_z$. The rotor COG is not exactly in the center of the stator, and therefore, some proportion of motor UMP forces will be seen because of the gyroscopic effect in a different plane; e.g., instead of a reaction to the overturning moment about the x-plane, the reaction will be seen in the y-plane. They are measured by the AMB signals as xy forces in the bearing planes, and together with the rotor tilting and bending mode effects, make the comparison of experimental and simulation results challenging.

VI. Conclusion

In a hermetic turbogenerator for a WHRS, the AMB-supported cage solid rotor IM offers a robust alternative to laminated cage IMs with traditional bearings. However, the system design requires consideration of disturbance forces and their possible impact on the AMB control.

This paper described the techniques to compute the UMP of solid rotor IMs in the FEM when eddy current and strong saturation effects cause transients in the rotor magnetization state. With variable gradually shortening time stepping, the steady-state rotor magnetization can be reached after 1.2–2 s. The total time depends on the rate of change of the time steps. The FEM-derived forces and experimentally measured bearing reaction forces to a combination of external disturbances, using the AMB control currents and built-in position sensors, were compared in the harmonic domain. These harmonic forces were incorporated into levitation control models, enabling a closed-loop detailed analysis. Simulation results of the effect of the IM UMP on AMB closed-loop operation were produced at a static eccentricity, which was dominant in the experimentation.

The computed static unbalance forces were mapped as a function of phase current, slip, and rotor angle. This allowed to construct a straightforward LUT engineering model. The effects of UMP on the complete closed-loop AMB–rotor system

in various eccentric and load conditions can be evaluated by using engineering LUT models in time simulations. For time closed-loop simulations, the LUT UMP and AMB models are superior in terms of accuracy and computational efficiency to, e.g., general harmonic models. The proposed methodology is applicable in system and control design.

It was found that for the modeled and tested operating conditions, the UMP from the prototype has no significant effect on the AMB–rotor control system performance. The IM and AMB planes are concentric up to about 0.1 mm. This small motor eccentricity, 2% of the nominal motor air gap, results in about 20 N dc and 4 N fundamental component differences between the measured 10% load acceleration and the motor-off deceleration. This trend is consistent with the simulation results from the FEM. For noncanned AMBs and different IM designs, clearances could result in significantly higher relative values of eccentricity. In such cases, the dominant UMP zero harmonic should be compared with the force capacity of the radial AMBs. The authors would recommend that the AMB force capacity remains four times as high as the worst-case value of the radial dc force computed as a sum of UMP, gravity, and other external forces. This is a general recommendation; the number would depend on various features of the closed-loop control system. Additionally, the UMP higher harmonics will propagate to the rotor positions and can potentially excite, e.g., the $1\mathrm{st}$ forward bending mode before reaching the $1\mathrm{st}$ critical speed (Fig. 13).

The derived models are general for most AMB–rotor systems. However, LUT force mapping of the UMP and AMBs has to be recalculated for each specific design.

The future work will include a closer analysis of the influence of the application, i.e., six degrees of motion of a ship on the bearing forces in a high-speed rotor. An enhanced AMB capacity can be achieved through new bearing materials and elimination of a canned design.

ACKNOWLEDGMENT

The author would like to thank Aument Power Oy for the opportunity to publish the results. Without all the efforts of technical and research teams at LUT testing of the prototype of that scale would not have been possible. The JMAG customer support advice is also acknowledged.

REFERENCES

[1] O. V. Thorsen and M. Dalva, "A survey of faults on induction motors in offshore oil industry, petrochemical industry, gas terminals, and oil refineries," *IEEE Trans. Ind. Appl.*, vol. 31, no. 5, pp. 1186–1196, Sep./Oct. 1995.

[2] H. Kim, J. Nerg, T. Choudhury, and J. T. Sopanen, "Rotordynamic simulation method of induction motors including the effects of unbalanced magnetic pull," *IEEE Access*, vol. 8, pp. 21631–21643, 2020.

[3] R. P. Jastrzebski, J. Vuojolainen, P. Jaatinen, T. Sillanpaa, and O. Pyrhonen, "Commissioning of modular 10 kW magnetically levitated test rig," in *Proc. IEEE 19th Int. Conf. Elect. Mach. Syst.*, 2016, pp. 1–6.

[4] R. Lateb, J. Enon, and L. Durantay, "High speed, high power electrical induction motor technologies for integrated compressors," in *Proc. IEEE Int. Conf. Elect. Mach. Syst.*, 2010, pp. 1–5.

[5] R. P. Jastrzebski, A. Putkonen, E. Kurvinen, and O. Pyrhonen, "Design and modeling of 2 MW AMB rotor with three radial bearing-sensor planes," *IEEE Trans. Ind. Appl.*, vol. 57, no. 6, pp. 6892–6902, Nov./Dec. 2021.

[6] R. P. Jastrzebski, K. Hynynen, A. Smirnov, and O. Pyrhonen, "Influence of the drive and dc link generated disturbances on an AMB control system," *PRZEGLAD ELEKTROTECHNICZNY (Elect. Rev.)*, vol. 88, no. 1a, pp. 247–252, 2012.

[7] T. P. Holopainen, A. Tenhunen, E. Lantto, and A. Arkkio, "Unbalanced magnetic pull induced by arbitrary eccentric motion of cage rotor in transient operation. part 1: Analytical model," *Elect. Eng.*, vol. 88, no. 1, pp. 13–24, 2005.

[8] D. G. Dorrell, A. Salah, and Y. Guo, "The detection and suppression of unbalanced magnetic pull in wound rotor induction motors using pole-specific search coils and auxiliary windings," *IEEE Trans. Ind. Appl.*, vol. 53, no. 3, pp. 2066–2076, May/Jun. 2017.

[9] J. Faiz, B. M. Ebrahimi, B. Akin, and H. A. Toliyat, "Comprehensive eccentricity fault diagnosis in induction motors using finite element method," *IEEE Trans. Magn.*, vol. 45, no. 3, pp. 1764–1767, Mar. 2009.

[10] B. Heller and V. Hamata, *Harmonic Field Effects in Induction Machines*. Amsterdam, The Netherlands: Elsevier, 1977.

[11] A. Laiho, K. Tammi, A. Burakov, A. Arkkio, and K. Zenger, "A built-in force actuator for active control of lateral rotor vibration in cage induction electrical machines," *J. Sound Vib.*, vol. 320, no. 3, pp. 496–515, Feb. 2009.

[12] D. G. Dorrell, "Sources and characteristics of unbalanced magnetic pull in three-phase cage induction motors with axial-varying rotor eccentricity," *IEEE Trans. Ind. Appl.*, vol. 47, no. 1, pp. 12–24, Jan./Feb. 2011.

[13] P. Frauman, A. Burakov, and A. Arkkio, "Effects of the slot harmonics on the unbalanced magnetic pull in an induction motor with an eccentric rotor," *IEEE Trans. Magn.*, vol. 43, no. 8, pp. 3441–3444, Aug. 2007.

[14] A. J. Fernandez Gomez, A. Dziechciarz, and T. J. Sobczyk, "Mathematical modeling of eccentricities in induction machines by the mono-harmonic model," in *Proc. IEEE 9th Int. Symp. Diagn. Electric Mach., Power Electron. Drives*, 2013, pp. 317–322.

[15] H. Chuan and J. K. H. Shek, "Calculation of unbalanced magnetic pull in induction machines through empirical method," *IET Electric Power Appl.*, vol. 12, pp. 1233–1239, 2018.

[16] J. J. R. Echeverria, P. V. V. Da Silva, and E. Da Costa Bortoni, "Analysis of orbital eccentricity and UMP in large salient pole synchronous machines," *IEEE Trans. Ind. Appl.*, vol. 55, no. 5, pp. 4715–4722, Sep./Oct. 2019.

[17] A. A. Salah, D. G. Dorrell, and Y. Guo, "A review of the monitoring and damping unbalanced magnetic pull in induction machines due to rotor eccentricity," *IEEE Trans. Ind. Appl.*, vol. 55, no. 3, pp. 2569–2580, May/Jun. 2019.

[18] A. Arkkio, *Analysis of Induction Motors Based on the Numerical Solution of the Magnetic Field and Circuit Equations*, no. 59. Acta Polytechnica Scandinavica, Electrical Engineering Series, 1987.

[19] F. W. Carter, "Air-gap induction," *Elect. World Eng.*, vol. 38, no. 22, pp. 884–888, 1901. [Online]. Available: http://perso.uclouvain.be/ernest.matagne/ELEC2311/SEM04/CARTER01.PDF

[20] A. C. Smith and D. G. Dorrell, "Calculation and measurement of unbalanced magnetic pull in cage induction motors with eccentric rotors. Part 2: Experimental investigation," *IEE Proc.: Electric Power Appl.*, vol. 143, no. 3, pp. 202–210, 1996.

[21] R. P. Jastrzebski, P. Jaatinen, A. Chiba, and O. Pyrhonen, "Design optimization of permanent magnet bearingless motor using differential evolution," in *Proc. IEEE 10th Annu. Energy Convers. Congr. Expo.*, 2018, pp. 2327–2334.

[22] R. P. Jastrzebski et al., "Automated design of AMB rotor systems with standard drive, control software and hardware technologies," in *Proc. 15th Int. Symp. Magn. Bearings (ISMB15)*, 2016, pp. 78–85.

[23] M. Antila, *Electromechanical Properties of Radial Active Magnetic Bearings*. Helsinki, Finland: Helsinki Univ. Technology, 1998.

[24] R. P. Jastrzebski, A. Smirnov, A. Mystkowski, and O. Pyrhonen, "Cascaded position-flux controller for an AMB system operating at zero bias," *Energies*, vol. 7, no. 6, pp. 3561–3575, 2014.

[25] A. Smirnov, R. P. Jastrzebski, and K. Hynynen, "Gain-scheduled and linear parameter-varying approaches in control of an active magnetic bearings," in *Proc. 12th Int. Symp. Magn. Bearings (ISMB12)*, 2010, pp. 350–360.

[26] *Mechanical Vibration - Vibration of Rotating Machinery Equipped with Active Magnetic Bearings - Part 3: Evaluation of Stability Margin*, Standard ISO 14839-3:2004(E), International Organisation for Standardization, Geneva, Switzerland, 2004.

[27] Y. H. Ha and J. A. Pearce, "A new window and comparison to standard windows," *IEEE Trans. Acoust., Speech, Signal Process.*, vol. 37, no. 2, pp. 298–301, Feb. 1989.

Rafal P. Jastrzebski (Senior Member, IEEE) was born in Lodz, Poland in 1978. He received the M.Sc. degree in electrical engineering from the Technical University of Lodz, Lodz, in 2002, and the D.Sc. degree in electrical engineering from the Lappeenranta University of Technology (LUT), Lappeenranta, Finland, in 2007. He was a Researcher with Poland, Germany, Japan, and Finland. He is currently an Associate Professor (tenured) with the University of Turku, Turku, Finland, and Docent with LUT Modelling and control of electromechanical systems. His research interests include mechatronic systems, digital control, energy applications, active magnetic bearings, magnetic levitation systems, and bearingless machines. From 2013 to 2018, he was an Academy Research Fellow. From 2009 to 2011, he was an Academy of Finland Postdoctoral Researcher.

Adam K. Pilat (Member, IEEE) was born in Krakow, Poland, in 1972. He received the M.Sc., Ph.D., and D.Sc. degrees in 1996, 2002 and 2014, respectively. He is currently a Professor with the AGH University of Science and Technology, Krakow, ów, Poland. He is also with the Department of Automatic Control and Robotics as a Researcher, didactic, and head of Photovoltaic, Robotics and Magnetic Levitation Laboratory. He is author and coauthor of 42 articles, 85 papers, four books, 12 book chapters, 20 patents. He is a Member of IEEE Control Systems Society and Robotics and Automation Society. His research interests include devices design, prototyping and control with embedded Active Magnetic Levitation technology, interdisciplinary modelling, simulation, controller synthesis, and real-time control.